ChemComm

COMMUNICATION

View Article Online
View Journal

Cite this: DOI: 10.1039/d1cc03171f

Received 16th June 2021,
Accepted 27th July 2021

DOI: 10.1039/d1cc03171f

rsc.li/chemcomm

Reconstructing two-dimensional defects in CuO nanowires for efficient CO_2 electroreduction to ethylene†

Jianfang Zhang,[ab] Zhengyuan Li,[b] Shuai Xia,[c] Tianyu Zhang,[b] Yan Wang,*[cd] Yucheng Wu*[cd] and Jingjie Wu*[b]

Here we report that *in situ* reconstructed Cu two-dimensional (2D) defects in CuO nanowires during CO_2RR lead to significantly enhanced activity and selectivity of C_2H_4 compared to the CuO nanoplatelets. Specifically, the CuO nanowires achieve high faradaic efficiency of 62% for C_2H_4 and a partial current density of 324 mA cm^{-2} yet at a low potential of −0.56 V *versus* a reversible hydrogen electrode. Structural evolution characterization and *in situ* Raman spectra reveal that the high yield of C_2H_4 on CuO nanowires is attributed to the *in situ* reduction of CuO to Cu followed by structural reconstruction to form 2D defects, *e.g.*, stacking faults and twin boundaries, which improve the CO production rate and *CO adsorption strength. This finding may provide a paradigm for the rational design of nanostructured catalysts for efficient CO_2 electroreduction to C_2H_4.

Electrochemical CO_2 reduction reaction (CO_2RR) provides a promising technology to convert CO_2 into fuels and value-added chemicals using renewable electricity.[1] Great progress has been made on the electrochemical CO_2RR since the seminal work by Hori *et al.*[2,3] To date, the mainstream research focus is still on the design of highly active and selective catalysts to produce a specific commodity product with high market price and size.[4] In particular, the electrochemical CO_2RR to C_{2+} products, including ethylene (C_2H_4) and ethanol (C_2H_5OH), has attracted increasing attention in the energy storage and chemical industry.[5]

Copper and copper oxides have been widely studied as efficient catalysts for electrochemical CO_2RR towards hydrocarbon products.[6] Despite the state-of-the-art Cu-based catalysts achieved a high C_2H_4 formation rate (>100 mA cm^{-2}) with faradaic efficiency (FE) > 60%, the high overpotential of C_2H_4 (<−0.80 V) on Cu catalysts requires massive energy input for practical and economic C_2H_4 production.[4,7–9] Thus, reducing the overpotential of CO_2RR catalysis remains an important objective that realizes industrial production of C_2H_4 under steady state conditions at a high current density (>200 mA cm^{-2}) and an appreciable selectivity (>60%).

The evolution of oxide-derived Cu nanostructures present various chemical state, residual oxygen, and crystalline defects when Cu oxides undergo electrochemical CO_2RR, which leads to an altered activity and selectivity of C_2H_4 relative to metallic Cu catalysts.[10,11] In particular, the crystalline defects in oxide-derived Cu catalysts have been proved as highly active sites for electrochemical CO_2RR towards C_2H_4 at low overpotentials.[12–14] Recently, the electrochemical reconstruction of Cu oxides has received increasing attention, which induced abundant grain boundary interfaces that lead to efficient electrochemical CO_2RR towards C_2H_4 production.[15–18] Apart from regular grain boundaries, stacking faults and twin boundaries in some metal nanostructures (*e.g.*, Ni-Co bimetal phosphide and Ag metal) have been demonstrated to be active for electrocatalysis of water splitting and CO_2-to-CO conversion.[19–21] Such two-dimensional (2D) defects involving stacking faults and twin boundaries in Cu are presumed to increase the yield of CO_2-to-C_2H_4 conversion while lowering overpotentials. The key to exploiting these particular 2D defects lies in developing a facile synthesis method to introduce stacking faults and twin boundaries. Controlling the morphology of Cu oxides can potentially induce stacking faults and twin boundaries during *in situ* electrochemical reconstructing process.

Here, we report that the CuO nanowires, distinguished from CuO nanoplatelets, tend to undergo *in situ* reconstruction to form 2D defects, including stacking faults and twin boundaries during electrochemical CO_2RR. Such abundant planar defects direct high-efficiency CO_2-to-C_2H_4 conversion. As a result, the

[a] *School of Instrument Science and Opto-electronics Engineering, Hefei University of Technology, Hefei 230009, China*
[b] *Department of Chemical and Environmental Engineering, University of Cincinnati, Cincinnati, OH 45221, USA. E-mail: jingjie.wu@uc.edu*
[c] *School of Materials Science and Engineering, Hefei University of Technology, Hefei 230009, China. E-mail: stone@hfut.edu.cn, ycwu@hfut.edu.cn*
[d] *China International S&T Cooperation Base for Advanced Energy and Environmental Materials & Anhui Provincial International S&T Cooperation Base for Advanced Energy Materials, Hefei University of Technology, Hefei 230009, China*

† Electronic supplementary information (ESI) available: Experimental section and supplementary figures. See DOI: 10.1039/d1cc03171f

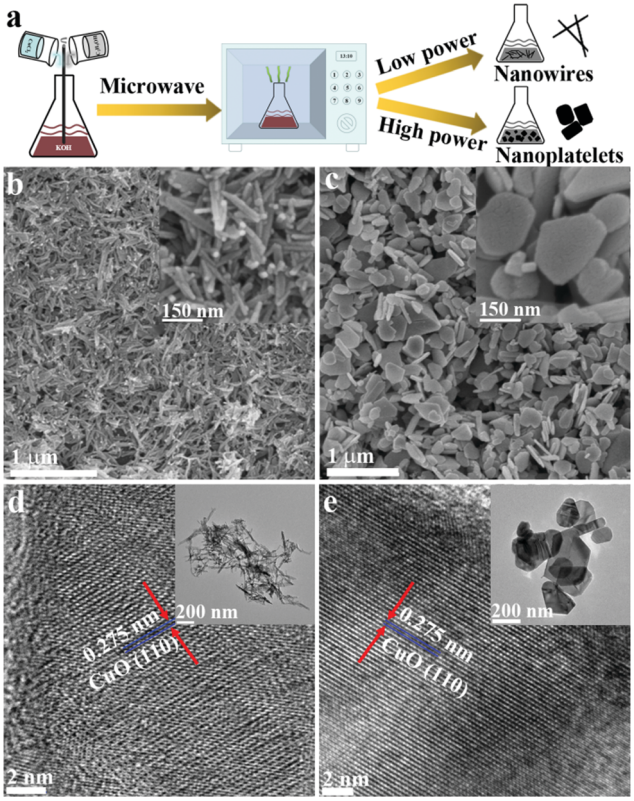

Fig. 1 (a) Schematic illustration for the synthetic process of CuO nanostructures; (b–e) SEM and HRTEM images of (b and d) CuO-1 and (c and e) CuO-4.

reduced CuO nanowires achieve a FE of 62% for C_2H_4 and a partial current density of 324 mA cm^{-2} at a low potential of −0.56 V (*versus* RHE, hereafter). *In situ* Raman spectra reveal that the 2D defects act as highly active sites that improve the adsorption of CO intermediates and consequently promote the *CO surface coverage and C–C coupling rate.

The CuO nanostructures as the Cu catalyst precursor were facilely synthesized by microwave heating $CuCl_2$ dissolved in 3 M KOH solution as illustrated in Fig. 1a. The microwave power determines the morphology of CuO nanostructures, *i.e.*, nanowires *versus* nanoplatelets (Fig. 1b, c and Fig. S1, ESI†). At a low power of 200 W, the obtained CuO-1 sample exhibited a uniform structure of nanowires with an average diameter of 20 nm (Fig. 1b). The nanowires became wider, accompanied by the formation of some nanoplatelets when the microwave power was increased to 300 W (CuO-2, Fig. S1a, ESI†). CuO nanoplatelets prevailed over nanowires as the power was increased to 400 W (CuO-3, Fig. S1b, ESI†). Further increasing the power to 500 W, pure CuO nanoplatelets were obtained, which had a lateral size of 150–300 nm and thickness of 30–50 nm (CuO-4, Fig. 1c). The crystalline structures of these four CuO samples were confirmed by XRD patterns (Fig. S2, ESI†). TEM images in the inset of Fig. 1d and e demonstrated the pure nanowires and nanoplatelets structures of CuO-1 and CuO-4, respectively. The corresponding high-resolution TEM (HRTEM) images showed clear lattice fringes with a lattice spacing of 0.275 nm for both CuO-1 and CuO-4, which was referred to the CuO(110) facets. The selective electron diffraction pattern suggests the single-crystal structure of CuO (Fig. S3, ESI†). The CuO-1 nanowires and CuO-4 nanoplatelets also exhibited a similar surface chemical state of exclusive Cu^{2+} as reflected by the XPS analysis of Cu 2p (Fig. S4a, ESI†), O 1s (Fig. S4b, ESI†), and Cu LMM (Fig. S4c, ESI†).[12,22] No K element was found in the CuO samples (Fig. S5, ESI†).

The electrocatalytic CO_2RR performance of as-prepared four CuO samples was studied in a customized flow cell using 1.0 M KOH as the catholyte. The electrolysis products were analyzed using gas chromatography (GC) and ^{1}H nuclear magnetic resonance (NMR). The CO_2RR current densities and CO_2 conversion progressively increased in order of CuO-1 > CuO-2 > CuO-3 > CuO-4 (Fig. S6 and S7, ESI†). It is also worth noting that the onset potential of CO_2RR rose from CuO-1 to CuO-4 electrodes. Regarding the product selectivity, CuO-1 electrode containing pure nanowires achieved the best FEs of C_{2+} products and the specific product of C_2H_4 (Fig. 2a, b and Fig. S8, ESI†). The CuO-1 electrode could reach the overall FE of C_{2+} products up to 81% at −0.56 V, where the FE of C_2H_4 achieved a maximum of 62% (Fig. 2a and b). The FEs of both C_{2+} products and C_2H_4 decreased when the fraction of nanoplatelets in CuO electrodes increased (Fig. 2b). The CuO-4 electrode with pure nanoplatelets exhibited the lowest FE of C_2H_4, which was only 38% at the same potential of −0.56 V. Moreover, the partial current densities of C_2H_4 ($j_{C_2H_4}$) showed the same tendency as the FE of C_2H_4 among the four CuO electrodes (Fig. 2c and Fig. S9, ESI†). The CuO-1 electrode achieved a high $j_{C_2H_4}$ of 324 and 418 mA cm^{-2} at −0.56 and −0.65 V, respectively, which were about 2.4 and 1.8 times as those of CuO-4 electrode at the equal potentials (Fig. 2c). Note that CuO-1 electrode achieved higher partial current density and FE of C_2H_4 under lower

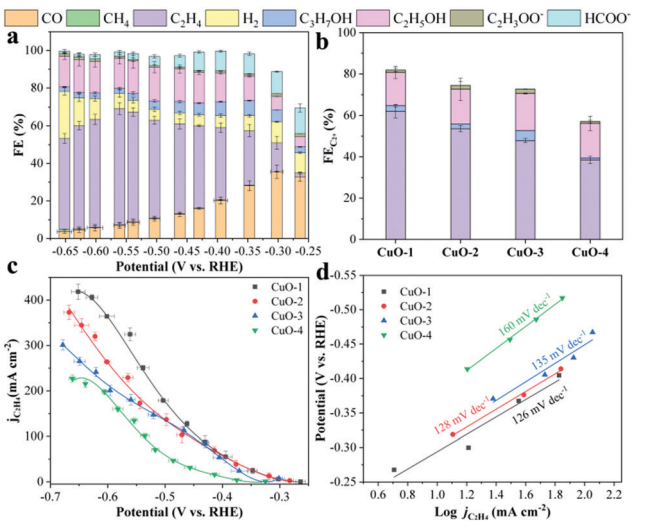

Fig. 2 Comparison of the CO_2 electro-reduction performance among different CuO electrodes. (a) Faradaic efficiencies of CuO-1 electrode as a function of potential; (b) the distribution of C_{2+} products at −0.56 V; (c) partial current density of C_2H_4 as a function of potential; and (D) Tafel plots.

overpotential than most reported Cu-based catalysts (Table S1, ESI†). Tafel plots for electrocatalytic CO_2-to-C_2H_4 conversion were investigated to explore the reaction kinetics of these CuO electrodes (Fig. 2d). Obviously, a significant difference in Tafel slopes towards C_2H_4 was observed on CuO-1 (126 mV dec^{-1}) and CuO-4 (160 mV dec^{-1}) electrodes, indicating the different rate-determining steps for CO_2-to-C_2H_4 conversion. We envisioned that such a significant difference in CO_2RR performance is attributed to the different morphologies of these CuO electrodes, leading to distinct behaviour of *in situ* structural evolution during CO_2RR.

Next, we probed the evolution of the structures and chemical composition of CuO electrodes after CO_2RR. The bulk structure remained intact for CuO-1 and CuO-4 electrodes after CO_2RR (Fig. 3). However, CuO species in these electrodes were fully reduced to metallic Cu after CO_2RR as shown by XRD results (Fig. S10, ESI†). The results of Cu 2p and Cu LMM revealed that the same fraction of Cu^+ species on the surfaces of nanowires and nanoplatelets after CO_2RR (Fig. S11, ESI†). The EDS mapping and spectrum of post CuO-1 electrode after CO_2RR also confirmed the coexistence of Cu and O elements (Fig. S12, ESI†), which is mainly ascribed to the easy re-oxidation of metallic Cu exposed to the air. Interestingly, lots of stacking faults were observed on CuO-1 nanowires together with some distinct twin boundaries of Cu (111) after CO_2RR as shown in HRTEM images (Fig. 3c and Fig. S13a, S14, ESI†). However, the CuO-4 nanoplatelets showed the integrity of lattice fringes of Cu (111) facet in HRTEM images (Fig. 3f and Fig. S13b, ESI†). The distinctive structural evolution of the CuO-1 nanowires and CuO-4 nanoplatelets during CO_2RR can be assigned to the different morphology and size between nanowires and nanoplatelets. The CuO-1 nanowires with smaller size at least in one dimension may be quickly reduced to metallic Cu, during which the surface undergoes reconstruction to form 2D defects. Based on the structural and chemical composition analysis of CuO electrodes after CO_2RR, we hypothesized that the reconstructed 2D defects, such as stacking faults and twin boundaries in nanowires, contribute to the highly active and selective CO_2-to-C_2H_4 conversion at low overpotentials.

To uncover the origin of the improved activity and selectivity towards C_2H_4 conversion on the reconstructed stacking faults and twin boundaries in the nanowires electrode, the effect of surface roughness should be considered first. The higher surface roughness was previously discovered to favor C_2H_4 formation.[23] The double-layer capacitances (C_{dl}) of the four CuO electrodes were calculated from the cyclic voltammetry (CV) curves in the non-faradaic reaction potential window at different scan rates (Fig. S15 and S16, ESI†). A capacitance of 3.36 mF cm^{-2} was obtained for the CuO-1 electrode, which was 1.40 times that of the CuO-4 electrode (2.38 mF cm^{-2}). The ECSA-normalized $j_{C_2H_4}$ of the CuO-1 electrode was still higher than that of the CuO-4 electrode (Fig. 4a and ESI†). Of note, the ratios of ECSA-normalized $j_{C_2H_4}$ between CuO-1 and CuO-4 electrodes were only 1.7 and 1.3 at potentials of −0.56 and −0.65 V, respectively. The ratios of C_2H_4 formation rate between these two electrodes were 2.4 and 1.8 at −0.56 and −0.65 V, respectively (Fig. S17, ESI†), much larger than the ratios of ECSA-normalized $j_{C_2H_4}$, indicating that the surface roughness cannot fully account for the improvement of C_2H_4 yield on the CuO-1 electrode. Further, we calculated the gross CO formation rates at different potentials over the different CuO electrodes (Fig. S18, ESI†). The gross CO molecule is the sum of coupled CO to generate C_{2+} products, hydrogenated CO to CH_4 and the remaining CO in the gas product stream (ESI†). As shown in Fig. 4b, the CuO-1 electrode achieved an ESCA-normalized CO formation rate of 1.9 mA cm^{-2} at −0.56 V, while the CuO-4 electrode only possessed 1.2 mA cm^{-2}, indicating an intrinsic faster CO generation rate on the CuO-1 electrode. The intrinsic faster CO generation rate will translate to a higher *CO

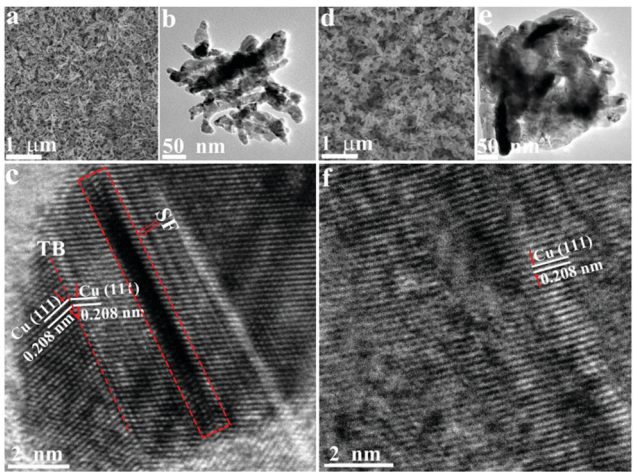

Fig. 3 SEM, TEM, and HRTEM images of (a–c) CuO-1 and (d–f) CuO-4 after the CO_2RR. SF: stacking faults; TB: twin boundary.

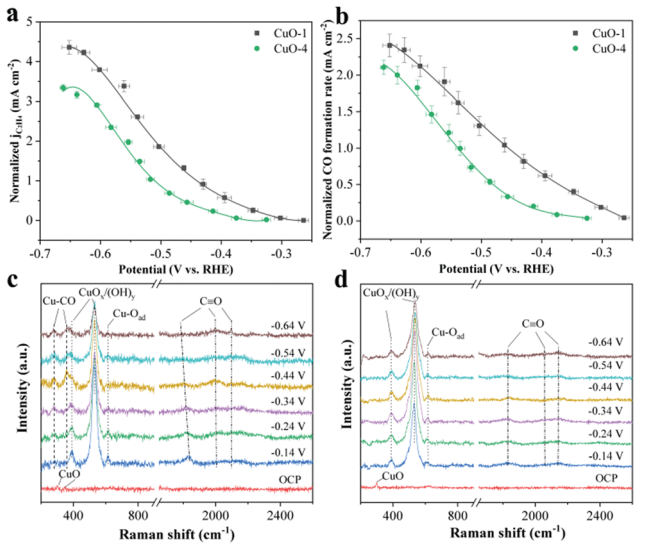

Fig. 4 (a) ECSA-normalized partial current density of C_2H_4 for CuO-1 and CuO-4 electrodes; (b) ECSA-normalized gross formation rate of CO on CuO-1 and CuO-4 electrodes; *in situ* Raman spectra of (c) CuO-1 and (d) CuO-4 electrodes at different applied potentials.

surface coverage, leading to the enhanced C–C coupling kinetics on the CuO-1 electrode.[23]

To reveal the faster kinetics of CO generation on the CuO-1 electrode, *in situ* Raman spectroscopy was carried out to probe the adsorption of key intermediates during CO_2RR (Fig. 4c and d). CuO peaks were only observed at the open circuit potential (OCP) on both CuO-1 and CuO-4 electrodes and then disappeared quickly upon applying potentials from −0.14 to −0.64 V. Two main peaks of $CuO_x/(OH)_y$ at 390 and 531 cm^{-1} were presented in both electrodes with a small shoulder peak of Cu–O_{ad} at 613 cm^{-1}.[24] As the applied potential exceeded −0.24 V, the CuO-1 electrode displayed two new peaks at 283 and 352 cm^{-1}, which are assigned to the restricted rotation of adsorbed *CO intermediates on Cu and the Cu-CO stretching, respectively.[9,25,26] On the contrary, those peaks could not be observed on the CuO-4 electrode even at more negative potentials, indicating a relatively lower *CO coverage relative to the CuO-1 electrode. The *in situ* Raman spectroscopy tests presented that the *CO intermediates could be sufficiently adsorbed on the CuO-1 electrode and facilitated the CO dimerization to form C_{2+} products.[9,27] Surface strain caused by stacking faults has been demonstrated by experimental and theoretical studies to upshift the d-band center of some noble metal (Au, Ag, and Pt), which increases the binding strength of reactive adsorbates on the catalyst surface.[28] The *CO binding energy also became stronger in stacking faults, leading to increasing *CO coverage on Cu surface and subsequently promoting C–C coupling for C_2H_4 production.[14] Therefore, the origin of higher *CO coverage on the CuO-1 electrode can be attributed to both increased *CO binding energy and faster kinetics of CO generation on stacking faults and twin boundaries.

In summary, our research shows the morphology dependence of Cu-based catalysts reconstruction during CO_2RR, which clarifies the significant difference in CO_2RR activity and selectivity toward C_{2+} products among many nanostructured Cu catalysts. CuO nanowires tend toward *in situ* reconstruction that forms enriched stacking faults and twin boundaries compared to nanoplatelets probably because CuO nanowires possess a smaller dimension than nanoplatelets. These 2D defects offer a higher intrinsic production rate of CO, leading to increased *CO surface coverage, along with higher adsorption energy of *CO, further increasing *CO surface coverage while promoting CO dimerization rate. As a result, CuO nanowires exhibit a high faradaic efficiency of 62% for C_2H_4 and a partial current density of 324 mA cm^{-2} yet at a low potential of −0.56 V.

This work was partially financially supported by NSF CBET-2033343. J. Z. thanks the support from National Natural Science Foundation of China (51772072, 51672065, U1810204). Y. W. and Y. W. would like to thank the financial support from the 111 Project (B18018).

Conflicts of interest

There are no conflicts to declare.

Notes and references

1 S. Nitopi, E. Bertheussen, S. B. Scott, X. Liu, A. K. Engstfeld, S. Horch, B. Seger, I. E. L. Stephens, K. Chan, C. Hahn, J. K. Norskov, T. F. Jaramillo and I. Chorkendorff, *Chem. Rev.*, 2019, **119**, 7610–7672.
2 Y. Y. Birdja, E. Pérez-Gallent, M. C. Figueiredo, A. J. Göttle, F. Calle-Vallejo and M. T. M. Koper, *Nat. Energy*, 2019, **4**, 732–745.
3 Y. Hori, K. Kikuchi and S. Suzuki, *Chem. Lett.*, 1985, 1695–1698.
4 R. I. Masel, Z. Liu, H. Yang, J. J. Kaczur, D. Carrillo, S. Ren, D. Salvatore and C. P. Berlinguette, *Nat. Nanotechnol.*, 2021, **16**, 118–128.
5 J. Resasco and A. T. Bell, *Trends Chem.*, 2020, **2**, 825–836.
6 C. Zhu, Z. Zhang, L. Zhong, C.-S. Hsu, X. Xu, Y. Li, S. Zhao, S. Chen, J. Yu, S. Chen, M. Wu, P. Gao, S. Li, H. M. Chen, K. Liu and L. Zhang, *Chem*, 2021, **7**, 406–420.
7 C.-T. Dinh, T. Burdyny, M. G. Kibria, A. Seifitokaldani, C. M. Gabardo, F. P. G. de Arquer, A. Kiani, J. P. Edwards, P. D. Luna, O. S. Bushuyev, C. Q. Zou, R. Quintero-Bermudez, Y. J. Pang, D. Sinton and E. H. Sargent, *Science*, 2018, **360**, 783–787.
8 F. Li, A. Thevenon, A. Rosas-Hernandez, Z. Wang, Y. Li, C. M. Gabardo, A. Ozden, C. T. Dinh, J. Li, Y. Wang, J. P. Edwards, Y. Xu, C. McCallum, L. Tao, Z. Q. Liang, M. Luo, X. Wang, H. Li, C. P. O'Brien, C. S. Tan, D. H. Nam, R. Quintero-Bermudez, T. T. Zhuang, Y. C. Li, Z. Han, R. D. Britt, D. Sinton, T. Agapie, J. C. Peters and E. H. Sargent, *Nature*, 2020, **577**, 509–513.
9 X. Chen, J. Chen, N. M. Alghoraibi, D. A. Henckel, R. Zhang, U. O. Nwabara, K. E. Madsen, P. J. A. Kenis, S. C. Zimmerman and A. A. Gewirth, *Nat. Catal.*, 2020, **4**, 20–27.
10 K. Zhao, Y. Liu, X. Quan, S. Chen and H. Yu, *ACS Appl. Mater. Interfaces*, 2017, **9**, 5302–5311.
11 C. W. Li and M. W. Kanan, *J. Am. Chem. Soc.*, 2012, **134**, 7231–7234.
12 H. Jung, S. Y. Lee, C. W. Lee, M. K. Cho, D. H. Won, C. Kim, H.-S. Oh, B. K. Min and Y. J. Hwang, *J. Am. Chem. Soc.*, 2019, **141**, 4624–4633.
13 Z. Q. Chen, T. Wang, B. Liu, D. F. Cheng, C. L. Hu, G. Zhang, W. J. Zhu, H. Y. Wang, Z. J. Zhao and J. L. Gong, *J. Am. Chem. Soc.*, 2020, **142**, 6878–6883.
14 C. Choi, T. Cheng, M. Flores Espinosa, H. Fei, X. Duan, W. A. Goddard, 3rd and Y. Huang, *Adv. Mater.*, 2019, **31**, e1805405.
15 Z. Xu, T. C. Wu, Y. Cao, C. C. Chen, X. R. Zeng, P. Lin and W. W. Zhao, *J. Catal.*, 2020, **383**, 42–50.
16 W. T. Osowiecki, J. J. Nussbaum, G. A. Kamat, G. Katsoukis, M. Ledendecker, H. Frei, A. T. Bell and A. P. Alivisatos, *ACS Appl. Energy Mater.*, 2019, **2**, 7744–7749.
17 Q. Lei, H. Zhu, K. P. Song, N. N. Wei, L. M. Liu, D. L. Zhang, J. Yin, X. L. Dong, K. X. Yao, N. Wang, X. H. Li, B. Davaasuren, J. J. Wang and Y. Han, *J. Am. Chem. Soc.*, 2020, **142**, 4213–4222.
18 H. S. Jeon, J. Timoshenko, C. Rettenmaier, A. Herzog, A. Yoon, S. W. Chee, S. Oener, U. Hejral, F. T. Haase and B. Roldan Cuenya, *J. Am. Chem. Soc.*, 2021, **143**, 7578–7587.
19 F. Hu, S. C. Abeyweera, J. Yu, D. Zhang, Y. Wang, Q. Yan and Y. Sun, *Chem*, 2020, **6**, 3007–3021.
20 Z. Li, J.-Y. Fu, Y. Feng, C.-K. Dong, H. Liu and X.-W. Du, *Nat. Catal.*, 2019, **2**, 1107–1114.
21 H. Liu, M. Jin, D. Zhan, J. Wang, X. Cai, Y. Qiu and L. Lai, *Appl. Catal., B*, 2020, **272**, 118951.
22 D. Gao, I. T. McCrum, S. Deo, Y.-W. Choi, F. Scholten, W. Wan, J. G. Chen, M. J. Janik and B. Roldan Cuenya, *ACS Catal.*, 2018, **8**, 10012–10020.
23 L. Wang, S. Nitopi, A. B. Wong, J. L. Snider, A. C. Nielander, C. G. Morales-Guio, M. Orazov, D. C. Higgins, C. Hahn and T. F. Jaramillo, *Nat. Catal.*, 2019, **2**, 702–708.
24 Y. Zhao, X. Chang, A. S. Malkani, X. Yang, L. Thompson, F. Jiao and B. Xu, *J. Am. Chem. Soc.*, 2020, **142**, 9735–9743.
25 C. Chen, X. Yan, S. Liu, Y. Wu, Q. Wan, X. Sun, Q. Zhu, H. Liu, J. Ma, L. Zheng, H. Wu and B. Han, *Angew. Chem., Int. Ed.*, 2020, **59**, 16459–16464.
26 J. Li, A. Ozden, M. Wan, Y. Hu, F. Li, Y. Wang, R. R. Zamani, D. Ren, Z. Wang, Y. Xu, D. H. Nam, J. Wicks, B. Chen, X. Wang, M. Luo, M. Graetzel, F. Che, E. H. Sargent and D. Sinton, *Nat. Commun.*, 2021, **12**, 2808.
27 J. Li, Z. Wang, C. McCallum, Y. Xu, F. Li, Y. Wang, C. M. Gabardo, C.-T. Dinh, T.-T. Zhuang, L. Wang, J. Y. Howe, Y. Ren, E. H. Sargent and D. Sinton, *Nat. Catal.*, 2019, **2**, 1124–1131.
28 M. C. Luo and S. J. Guo, *Nat. Rev. Mater.*, 2017, **2**, 17059.

